



## Oxygen vacancies engineering of Fe doped LaCoO<sub>3</sub> perovskite catalysts for efficient H<sub>2</sub>S selective oxidation

Xiaohai Zheng <sup>a,b</sup>, Bang Li <sup>a</sup>, Lijuan Shen <sup>d</sup>, Yanning Cao <sup>a,b,\*</sup>, Yingying Zhan <sup>a,b,\*</sup>, Shoutian Zheng <sup>c,\*\*</sup>, Shiping Wang <sup>a,b</sup>, Lilong Jiang <sup>a,b</sup>

<sup>a</sup> National Engineering Research Center of Chemical Fertilizer Catalyst, Fuzhou University, Fuzhou, Fujian 350002, China

<sup>b</sup> Qingyuan Innovation Laboratory, Quanzhou, Fujian 362801, China

<sup>c</sup> State Key Laboratory of Photocatalysis on Energy and Environment, College of Chemistry, Fuzhou University, Fuzhou, Fujian 350108, China

<sup>d</sup> College of Environmental Science and Engineering, Fujian Normal University, Fuzhou, Fujian 350007, China



### ARTICLE INFO

#### Keywords:

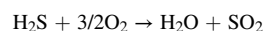
LaCoO<sub>3</sub> perovskite  
Fe doped  
Oxygen vacancy  
Density functional theory  
H<sub>2</sub>S selective oxidation

### ABSTRACT

Fe-doped LaCoO<sub>3</sub> perovskite catalysts synthesized via a facile citric acid-assisted sol-gel route have been applied for the H<sub>2</sub>S selective oxidation. The as-synthesized LaFe<sub>x</sub>Co<sub>1-x</sub>O<sub>3</sub> perovskites exhibit a randomly macroporous structure formed by the accumulation of nanoparticles. Characterization studies reveal that appropriate Fe substitution effectively enhances the formation of oxygen vacancies, and thus improves the lattice oxygen mobility and H<sub>2</sub>S adsorbability, respectively. The obtained LaFe<sub>0.4</sub>Co<sub>0.6</sub>O<sub>3</sub> exhibited remarkable catalytic activity, with the H<sub>2</sub>S conversion and sulfur yield of 100% at 190 °C. A combined approach of *in-situ* FT-IR and *in-situ* Raman experiments disclosed that the plausible reaction pathway of H<sub>2</sub>S selective oxidation over LaFe<sub>x</sub>Co<sub>1-x</sub>O<sub>3</sub> perovskites follows the Mars-van Krevelen mechanism. The density functional theory calculations revealed that Fe-doping improves the formation of oxygen vacancy and enhances the adsorption of H<sub>2</sub>S. This study offers new insights for the design of highly efficient perovskites for the selective oxidation of H<sub>2</sub>S.

### 1. Introduction

Hydrogen sulfide (H<sub>2</sub>S), is a highly toxic and noxious air pollutant produced from chemical processes such as coal chemicals, oil refinery and natural gas exploitation [1,2]. Owing to the extreme toxicity and corrosiveness, the proper removal of H<sub>2</sub>S before its emission is of critical importance to environmental protection and industrial production. The Claus technology is commonly utilized to convert H<sub>2</sub>S into elemental sulfur in industrial processes [3]. Nevertheless, limited by thermodynamics, about 2–5% of H<sub>2</sub>S still maintains in the off-gas [4]. Among the developed desulfurization processes, selective oxidation of H<sub>2</sub>S is highly promising due to low capital requirement and thermodynamic completeness [5]. The reaction equations of H<sub>2</sub>S selective oxidation are as follows (Eq. (1) is the main reaction, Eqs. (2) and (3) are the side reactions) [6]:



Metal oxides, such as Fe<sub>2</sub>O<sub>3</sub>, Al<sub>2</sub>O<sub>3</sub> and V<sub>2</sub>O<sub>5</sub>, were applied for the selective oxidation of H<sub>2</sub>S but the results were far from perfect [7]. For instance, the low selectivity of Fe<sub>2</sub>O<sub>3</sub> and the high toxicity of V<sub>2</sub>O<sub>5</sub> are the main issues that prevent them from widespread applications [8].

Owing to the diverse chemical properties and high electron mobility, the metal oxide perovskite materials with ABO<sub>3</sub> structure have been studied in various catalytic reactions [9,10]. However, limited by weak oxygen mobility, the perovskite oxides exhibit poor catalytic performance for the oxidation reaction. Our previous works proved that the presence of oxygen vacancies could enhance oxygen mobility [11]. Benefiting from the excellent structural stability, the A or B site of perovskite could be substituted by foreign cations with different ionic radii, leading to the generation of crystal distortions and abundant oxygen vacancies [12]. For example, Zheng et al. introduced boron species into LaCoO<sub>3</sub> perovskites by sol-gel method, which induces the distortion of LaCoO<sub>3</sub> structure and creates oxygen vacancies [13]. As a result, the

\* Corresponding authors at: National Engineering Research Center of Chemical Fertilizer Catalyst, Fuzhou University, Fuzhou, Fujian 350002, China.

\*\* Corresponding author.

E-mail addresses: [yncao@fzu.edu.cn](mailto:yncao@fzu.edu.cn) (Y. Cao), [zhanyingying@fzu.edu.cn](mailto:zhanyingying@fzu.edu.cn) (Y. Zhan), [stzheng@fzu.edu.cn](mailto:stzheng@fzu.edu.cn) (S. Zheng).

boron-dispersed LaCoO<sub>3</sub> exhibited high catalytic performance for C<sub>3</sub>H<sub>8</sub> oxidation. Meanwhile, Co<sub>3</sub>O<sub>4</sub> is rich in oxygen vacancies and Fe-based materials are active for the H<sub>2</sub>S selective oxidation [14]. For instance, Sun et al. reported the synthesis of cobalt decorated N-doped hollow carbon nanofibers (Co-NHCFs) for H<sub>2</sub>S selective oxidation. The introduction of cobalt enhances the formation of reactive oxygen species, further promoting the catalytic activity of H<sub>2</sub>S oxidation [15]. Therefore, it is promising to fabricate a desired catalyst by combining the advantages of perovskites and the prominent properties of iron and cobalt. Moreover, Fe-doped LaCoO<sub>3</sub> perovskite has rarely been studied in the H<sub>2</sub>S selective oxidation.

In the present work, a series of LaFe<sub>x</sub>Co<sub>1-x</sub>O<sub>3</sub> perovskite catalysts were prepared by a facile citric acid sol-gel route, and tested in H<sub>2</sub>S selective oxidation. The doping of Fe species into the LaCoO<sub>3</sub> crystal lattices induces the formation of oxygen vacancies without destroying the perovskite structure, which improves the process of reactant adsorption and dissociation. Simultaneously, the formed oxygen vacancies could promote the migration of oxygen species, thus facilitating the oxidation of H<sub>2</sub>S. *In-situ* FT-IR and *in-situ* Raman experiments were further performed to disclose the mechanism of H<sub>2</sub>S oxidation over LaFe<sub>x</sub>Co<sub>1-x</sub>O<sub>3</sub> perovskites. This work may provide new guidance for the design of efficient perovskites for H<sub>2</sub>S selective oxidation.

## 2. Materials and methods

### 2.1. Synthesis of catalysts

LaFe<sub>x</sub>Co<sub>1-x</sub>O<sub>3</sub> perovskites were synthesized as follows: 3.75 mmol of Co(OAc)<sub>2</sub>·4H<sub>2</sub>O, 3.75 mmol of La(NO<sub>3</sub>)<sub>3</sub>·6H<sub>2</sub>O and a certain amount of Fe(NO<sub>3</sub>)<sub>3</sub>·9H<sub>2</sub>O were dissolved in 40 mL of aqueous solution (a mixture containing 4 mL of HNO<sub>3</sub>, 16 mmol of CO(NH<sub>2</sub>)<sub>2</sub> and 16 mmol of citric acid). The mixed solution was stirred at 35 °C for 15 min, then it was heated to 80 °C and kept at this temperature until a gel was formed. The obtained solution was dried at 120 °C for 20 h in an oven to form a dry gel. The resulting gel was put in a furnace with the calcination at 600 °C for 6 h. The final samples were named as LaFe<sub>x</sub>Co<sub>1-x</sub>O<sub>3</sub> (x = 0, 0.2, 0.4 or 0.6). To ensure the purity and crystallinity of perovskites, cobalt acetate was used instead of cobalt nitrate in the synthesis process because of the chelation of CH<sub>3</sub>COO<sup>-</sup> ions.

### 2.2. Instrumental characterizations

The X-ray powder diffraction (XRD) patterns were obtained by a Bruker D8-Advance X-ray diffractometer with Cu K $\alpha$  radiation (40 mA, 45 kV). The transmission electron microscopy (TEM) and high-resolution TEM (HRTEM) images were taken by a JEOL-JEM-2011 microscope equipped with energy-dispersive X-Ray spectroscopy (EDX) operated at 200 kV. The scanning electron microscopy (SEM) images were acquired on a Hitachi S-4800 field-emission microscope. The N<sub>2</sub> adsorption-desorption isotherms were determined by a 3Flex analyzer (Micromeritics). The X-ray photoelectron spectrometry (XPS) spectra were acquired by an ESCALab MKII X spectrometer. Inductively coupled plasma optical emission spectrometry (ICP-OES) was conducted on a Perkin-Elmer Optima 8000 to analyze the content of metal elements. The electron paramagnetic resonance (EPR) experiment was performed by a Bruker A300 spectrometer provided by Sci-go Instrument Testing Platform. The temperature-programmed desorption of oxygen (O<sub>2</sub>-TPD) and H<sub>2</sub>-temperature programmed reduction (H<sub>2</sub>-TPR) experiments were performed using a Micromeritics Autochem 2920II chemisorption analyzer. The normal and *in-situ* Fourier transform infrared (FT-IR) spectra were collected by a Thermo Fisher Nicolet 6700 spectrometer. The normal and *in-situ* Raman spectra were acquired by a Renishaw Viat spectrometer with a laser beam of  $\lambda$  = 532 nm. Further details on the characterization procedures were provided in the Supporting Information.

### 2.3. Catalytic activity evaluation

The catalytic activity of the perovskites was evaluated for H<sub>2</sub>S selective oxidation. The experiments were performed in a continuous fixed-bed quartz reactor (Fig. S1). Typically, 0.2 g catalyst (40–60 meshes) was loaded into a quartz reactor with a 7 mm inner diameter. The feed gas consisting of 2500 ppm O<sub>2</sub> and 5000 ppm H<sub>2</sub>S balanced by N<sub>2</sub> was fed into the reactor at 30 mL·min<sup>-1</sup> with a weight hourly space velocity (WHSV) of 9000 mL·g<sup>-1</sup>·h<sup>-1</sup> (T = 90–220 °C). Each temperature point was held for 60 min before H<sub>2</sub>S conversion was recorded. To trap the formed sulfur in the off-gas, a condenser with ice water was placed downstream of the reactor. A gas chromatography (GC9720II) equipped with TC-detector was applied to analyze the outlet gases. The H<sub>2</sub>S conversion (X<sub>H<sub>2</sub>S</sub>), S selectivity (S<sub>sulfur</sub>) and S yield were defined as follows:

$$X_{H_2S} = \frac{(H_2S)_{in} - (H_2S)_{out}}{(H_2S)_{in}} \times 100\% \quad (4)$$

$$S_{sulfur} = \frac{(H_2S)_{in} - (H_2S)_{out} - (SO_2)_{out}}{(H_2S)_{in} - (H_2S)_{out}} \times 100\% \quad (5)$$

$$\text{Sulfur yield} = (X_{H_2S}) \times (S_{sulfur}) \quad (6)$$

The reaction rate (r<sub>H<sub>2</sub>S</sub>) was calculated as follows:

$$r_{H_2S} = \frac{X_{H_2S} \times C \times V_{gas}}{22.4 m_{cat}} \left( mol \cdot g^{-1} \cdot s^{-1} \right) \quad (7)$$

Where X<sub>H<sub>2</sub>S</sub> and m are the H<sub>2</sub>S conversion at 220 °C and the catalyst mass. C and V<sub>gas</sub> represent the H<sub>2</sub>S concentration and molar flow rate in the inlet gas.

### 2.4. DFT calculations

All spin-polarized DFT calculations were carried out by employing the Vienna *ab initio* simulation package (VASP) [16,17]. The generalized gradient approximation of Perdew-Burke-Ernzerhof (PBE) exchange-correlation functional was employed, and the interactions between electron and ion were described by the projector augmented wave (PAW) potentials. The PBE plus on-site repulsion U (PBE+U) method was adopted to properly treat the electron correlation of partially occupied Co and Fe 3d states, and the U<sub>eff</sub> parameters of 3.0 and 4.0 eV were used respectively. The kinetic energy cut-off for the plane-wave expansion was set to 400 eV.

## 3. Results and discussions

### 3.1. Structural and morphological characteristics

Fig. 1A shows the XRD patterns of the obtained LaCoO<sub>3</sub> synthesized by the sol-gel method. The diffraction peaks of the product correspond to a typical rhombohedral perovskite LaCoO<sub>3</sub> phase (JCPDS No. 48-0123, R-3c). The absence of La or Co oxides implies the presence of a pure LaCoO<sub>3</sub> phase. As Co is gradually substituted by Fe, the diffraction peaks shift to small angles (Fig. S2). This phenomenon is due to the ion radius of Fe<sup>3+</sup> (0.64 Å) being larger than that of Co<sup>3+</sup> (0.61 Å). This indicates that the substitution of Co by Fe in the LaCoO<sub>3</sub> lattice leads to the increase of crystal interplanar distances and lattice distortion [18]. In ABO<sub>3</sub> perovskite oxides, the B sites with six-fold coordination may be occupied by transition-metal cations with r<sub>B</sub> > 0.51 Å [19]. Owing to the high stability of perovskite structure, B site cations could be partially substituted by metals with different oxidation states. As a result, structural defects including cationic or anionic vacancies will be formed in the perovskite structure. The tolerance factor of ABO<sub>3</sub> type perovskite is a useful crystal-chemistry tool, which is expressed as t = (r<sub>O</sub> + r<sub>A</sub>)/ $\sqrt{2}$ ·(r<sub>O</sub> + r<sub>B</sub>) (r<sub>O</sub>, r<sub>A</sub> and r<sub>B</sub> represent the ion radii of O, A and B ions)

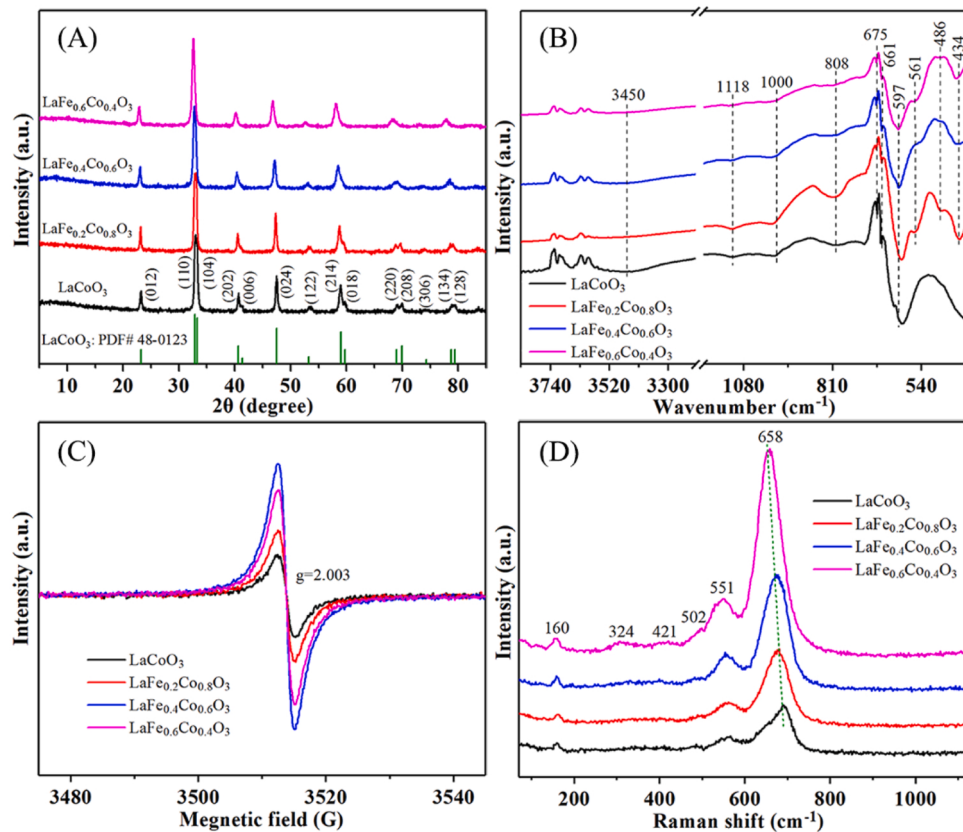


Fig. 1. (A) XRD patterns, (B) FT-IR spectra, (C) EPR spectra and (D) Raman spectra of LaFe<sub>x</sub>Co<sub>1-x</sub>O<sub>3</sub> perovskite catalysts.

[20]. According to the formula, perovskite could be formed as long as  $0.8 \leq t \leq 1$  is satisfied. Due to the larger ionic radius of Fe<sup>3+</sup> than that of Co<sup>3+</sup> (the radii of La<sup>3+</sup>, Co<sup>3+</sup>, Fe<sup>3+</sup> and O<sup>2-</sup> are 1.03, 0.61, 0.64 and 1.40 Å, respectively), the tolerance factors decrease with the Fe doping (Table 1). Meanwhile, the calculated tolerance factors indicate that they still possess stable perovskite structures. The decrease in tolerance factors means that Fe doping facilitates the formation of structural defects [21]. It is noted that the signals of Fe oxides cannot be found over the LaFe<sub>0.2</sub>Co<sub>0.8</sub>O<sub>3</sub>, LaFe<sub>0.4</sub>Co<sub>0.6</sub>O<sub>3</sub>, and LaFe<sub>0.6</sub>Co<sub>0.4</sub>O<sub>3</sub>, which suggests that the Fe species are too small to be detected or finely dispersed in the catalysts. In addition, the crystallite size of catalysts was calculated by the Scherrer equation, which follows the order of LaFe<sub>0.6</sub>Co<sub>0.4</sub>O<sub>3</sub> < LaFe<sub>0.4</sub>Co<sub>0.6</sub>O<sub>3</sub> < LaFe<sub>0.2</sub>Co<sub>0.8</sub>O<sub>3</sub> < LaCoO<sub>3</sub>. The result implies that the incorporation of Fe ions hinders the grain growth of LaFe<sub>x</sub>Co<sub>1-x</sub>O<sub>3</sub>. The textural characteristics of the LaFe<sub>x</sub>Co<sub>1-x</sub>O<sub>3</sub> perovskites were depicted in Fig. S3. The adsorption isotherms (Fig. S3A) of LaFe<sub>x</sub>Co<sub>1-x</sub>O<sub>3</sub> catalysts could be ascribed to IV-type with an H3 hysteresis loop, reflecting the rich mesoporous structure. As presented in Fig. S3B, the pore size distributions of catalysts also confirm the mesoporous structure of LaFe<sub>x</sub>Co<sub>1-x</sub>O<sub>3</sub> perovskites. The textural properties of catalysts (Table 1) indicate that Fe-doping has little effect on the pore volume and specific surface area of LaCoO<sub>3</sub> perovskite.

Table 1  
Tolerance factor, crystal size and textural properties of LaFe<sub>x</sub>Co<sub>1-x</sub>O<sub>3</sub> perovskites.

Samples	Tolerance factor (nm)	Crystal size	Surface area (m <sup>2</sup> /g)	Pore volume (cm <sup>3</sup> /g)	Pore size (nm)
LaCoO <sub>3</sub>	0.8549	33.4	14.8	0.082	20.7
LaFe <sub>0.2</sub> Co <sub>0.8</sub> O <sub>3</sub>	0.8524	30.8	16.5	0.084	18.6
LaFe <sub>0.4</sub> Co <sub>0.6</sub> O <sub>3</sub>	0.8499	27.6	17.4	0.091	16.5
LaFe <sub>0.6</sub> Co <sub>0.4</sub> O <sub>3</sub>	0.8474	25.9	17.7	0.093	14.8

The functional groups of LaFe<sub>x</sub>Co<sub>1-x</sub>O<sub>3</sub> perovskites were investigated by FT-IR analysis (Fig. 1B). As for LaCoO<sub>3</sub>, the absorption peak at ca. 410, 594 and 661 cm<sup>-1</sup> are assigned to the Co-O stretching vibration (E<sub>u</sub> vibration mode), La-O-Co stretching vibration (A<sub>2u</sub> vibration mode) and La-O vibration [22]. The peaks at 675 and 808 cm<sup>-1</sup> are ascribed to the Co-O bending vibration ( $\delta_{O-Co-O}$ ) and Co-O-Co vibration, respectively. The peaks at 1000–1118 and 3450 cm<sup>-1</sup> are related to the distortion in H<sub>2</sub>O and OH stretching vibration. For LaFe<sub>x</sub>Co<sub>1-x</sub>O<sub>3</sub> perovskites, new peaks appear at 486 and 561 cm<sup>-1</sup>, which correspond to the stretching mode of Fe-O bonds [23]. Compared with LaCoO<sub>3</sub>, the peaks of LaFe<sub>x</sub>Co<sub>1-x</sub>O<sub>3</sub> perovskites at around 410 and 594 cm<sup>-1</sup> exhibit a blue shift to the larger wave numbers, suggesting that the force constants (*k*) of Co-O and Co-O-La bonds are decreased [24]. This result demonstrates that Fe-doping causes lattice distortion and therefore leads to better surface oxygen migration. To determine the surface defect state in LaFe<sub>x</sub>Co<sub>1-x</sub>O<sub>3</sub> catalysts, the EPR technique was performed and the obtained spectra are illustrated in Fig. 1C. Obviously, all of the catalysts display a strong axial sign at  $g_{av}=2.003$ , which is related to the superoxide anion (O<sup>2-</sup>) signal [25]. The peak intensity of the catalysts follows the order of LaFe<sub>0.4</sub>Co<sub>0.6</sub>O<sub>3</sub> > LaFe<sub>0.6</sub>Co<sub>0.4</sub>O<sub>3</sub> > LaFe<sub>0.2</sub>Co<sub>0.8</sub>O<sub>3</sub> > LaCoO<sub>3</sub>, indicating the highest number of surface oxygen defects of LaFe<sub>0.4</sub>Co<sub>0.6</sub>O<sub>3</sub>. The abundant oxygen defects would facilitate the activation of oxygen species over LaFe<sub>x</sub>Co<sub>1-x</sub>O<sub>3</sub> catalysts.

The structural information of LaFe<sub>x</sub>Co<sub>1-x</sub>O<sub>3</sub> catalysts was further investigated by Raman spectra. As displayed in Fig. 1D, LaCoO<sub>3</sub> exhibits five bands located at 160, 410, 485, 558 and 689 cm<sup>-1</sup>. In detail, the band at 160 cm<sup>-1</sup> is ascribed to the E<sub>g</sub> vibration mode of La atoms along *a* and *b* axis. The peaks at 410, 485 and 558 cm<sup>-1</sup> are related to the E<sub>g</sub> bending mode, semiconducting state and E<sub>g</sub> quadrupole mode of LaCoO<sub>3</sub>. The strong Raman peak at 689 cm<sup>-1</sup> corresponds to the Co-O stretching vibration [26]. In addition, Fe-modified LaCoO<sub>3</sub> catalysts exhibit a new peak at 324 cm<sup>-1</sup>, which could be attributed to the Fe-O stretching mode. It is accepted that the change of the Raman band at

ca. 689 cm<sup>-1</sup> is related to the change of mean Co-O bond length, which may result from the epitaxial strain-induced structure distortion of CoO<sub>6</sub> regular octahedrons. With the increase of Fe content, the position of Co-O stretching vibration over LaFe<sub>x</sub>Co<sub>1-x</sub>O<sub>3</sub> catalysts shifts to the lower wavenumbers, which indicates an increase in the mean Co-O bond length [27]. This result weakens the Co-O bonds and finally promotes the reactivity of the lattice oxygen.

The electronic structure and elements state of the targeted LaFe<sub>x</sub>Co<sub>1-x</sub>O<sub>3</sub> catalysts are characterized by XPS. The survey scans illustrated in Fig. 2A show that the LaFe<sub>x</sub>Co<sub>1-x</sub>O<sub>3</sub> perovskites exhibit the typical signals of La, Fe, O and Co elements. As for Co 2p spectra (Fig. 2B), the Co 2p<sub>3/2</sub> and Co 2p<sub>1/2</sub> peaks split into two pairs of signals, which correspond to Co<sup>3+</sup> (779.8/794.6 eV) and Co<sup>2+</sup> (782.3/796.2 eV) species [28]. The Co<sup>2+</sup>/Co<sup>3+</sup> ratio calculated by the integrated XPS peak area follows the sequence of LaFe<sub>0.4</sub>Co<sub>0.6</sub>O<sub>3</sub> (0.77) > LaFe<sub>0.6</sub>Co<sub>0.4</sub>O<sub>3</sub> (0.72) > LaFe<sub>0.2</sub>Co<sub>0.8</sub>O<sub>3</sub> (0.67) < LaCoO<sub>3</sub> (0.64), indicating that Co<sup>2+</sup> species could be enriched on the surface by Fe substitution. Additionally, the Co 2p peaks shifts to the larger BEs, which is caused by the variation of Co<sup>3+</sup> → Co<sup>2+</sup>. The Fe 2p XPS spectra of LaFe<sub>x</sub>Co<sub>1-x</sub>O<sub>3</sub> perovskites display two peaks at Fe 2p<sub>1/2</sub> and Fe 2p<sub>3/2</sub> at 723.3 and 710.9 eV, which could be divided into eight peaks by spin-orbit splitting (Fig. 2C). The peak at about 709.3 eV is related to the Fe<sup>2+</sup> species, and the presence of Fe<sup>2+</sup> is due to the redox equilibrium of Fe<sup>3+</sup> + Co<sup>2+</sup> ⇌ Fe<sup>2+</sup> + Co<sup>3+</sup> [29]. It is obvious that the majority of Fe species on the LaFe<sub>x</sub>Co<sub>1-x</sub>O<sub>3</sub> perovskites surface is trivalent.

As presented in Fig. 2D, O 1s XPS spectra are deconvoluted into two peaks at ca. 528.9 and 531.1 eV, which could be identified as lattice oxygen (O<sub>lat</sub>) and chemisorbed oxygen (O<sub>ads</sub>) species. In the ABO<sub>3</sub> perovskites, the O<sub>ads</sub> content corresponds to the oxygen vacancies concentration [30]. The relative O<sub>ads</sub> content, defined as O<sub>ads</sub>/O<sub>total</sub>, is calculated by integrating the peak area of the XPS spectra. The calculated results indicate that LaFe<sub>0.4</sub>Co<sub>0.6</sub>O<sub>3</sub> shows the largest O<sub>ads</sub>/O<sub>total</sub> value (0.64), followed by LaFe<sub>0.6</sub>Co<sub>0.4</sub>O<sub>3</sub> (0.61) and LaFe<sub>0.2</sub>Co<sub>0.8</sub>O<sub>3</sub> (0.59).

(0.59), with LaCoO<sub>3</sub> (0.57) the least active. The obtained data imply the richness of oxygen vacancies in LaFe<sub>0.4</sub>Co<sub>0.6</sub>O<sub>3</sub>. It is worth noting that O 1s BE of LaFe<sub>0.4</sub>Co<sub>0.6</sub>O<sub>3</sub> shifts to a lower value than other catalysts. The phenomenon is due to the increase of electron density around oxygen species resulting from Fe-doping, and that eventually causes the oxygen to become more active [31]. The La 3d XPS spectra presented in Fig. S4 show that the La 3d<sub>5/2</sub> and La 3d<sub>3/2</sub> peaks are located at around 833.7 and 850.5 eV (spin-orbital splitting of 16.8 eV) with their satellite peaks at about 837.9 and 854.5 eV. These values imply that La<sup>3+</sup> ions are the main lanthanum species in the LaFe<sub>x</sub>Co<sub>1-x</sub>O<sub>3</sub> perovskite [32].

As presented in Fig. 3, LaFe<sub>x</sub>Co<sub>1-x</sub>O<sub>3</sub> catalysts exhibit well-defined morphology with agglomeration of submicron particles. There are some gaps and voids in the net structure of catalysts formed by the gridding of fused particles. The formation of gaps and voids could be due to the exfoliation of the final product and the release of CO<sub>2</sub> during calcination. The particles of LaCoO<sub>3</sub> appear to be denser than those of LaFe<sub>x</sub>Co<sub>1-x</sub>O<sub>3</sub> catalysts. As for LaFe<sub>0.6</sub>Co<sub>0.4</sub>O<sub>3</sub>, the well-defined morphology has suffered a destroy. The network structure with abundant voids and gaps is conducive to the easy access of reactants to active sites [33].

TEM characterization was applied to further analyse the detailed structure of LaFe<sub>0.4</sub>Co<sub>0.6</sub>O<sub>3</sub>. As presented in Fig. 4A, LaFe<sub>0.4</sub>Co<sub>0.6</sub>O<sub>3</sub> possesses a randomly macroporous structure formed by the accumulation of nanoparticles, which is in consistent with the SEM result. Meanwhile, the mean particle size of irregular nanoparticle is about 40 nm (Fig. 4B). The HRTEM image (Fig. 4C) display distinct interplanar distance of 0.27 and 0.38 nm, which are ascribed to the (110) and (012) planes of rhombohedral LaCoO<sub>3</sub> [34], respectively. Additionally, an obvious crystal defect is found (as indicated by a red circle), which may be formed by Fe-doping. The EDX mapping images shown in Fig. 4D indicate that La, Co, O and Fe species are uniformly dispersed on the LaFe<sub>0.4</sub>Co<sub>0.6</sub>O<sub>3</sub>. Moreover, the mole content of metal elements in LaFe<sub>x</sub>Co<sub>1-x</sub>O<sub>3</sub> perovskites was determined by ICP-OES (Table S1). The

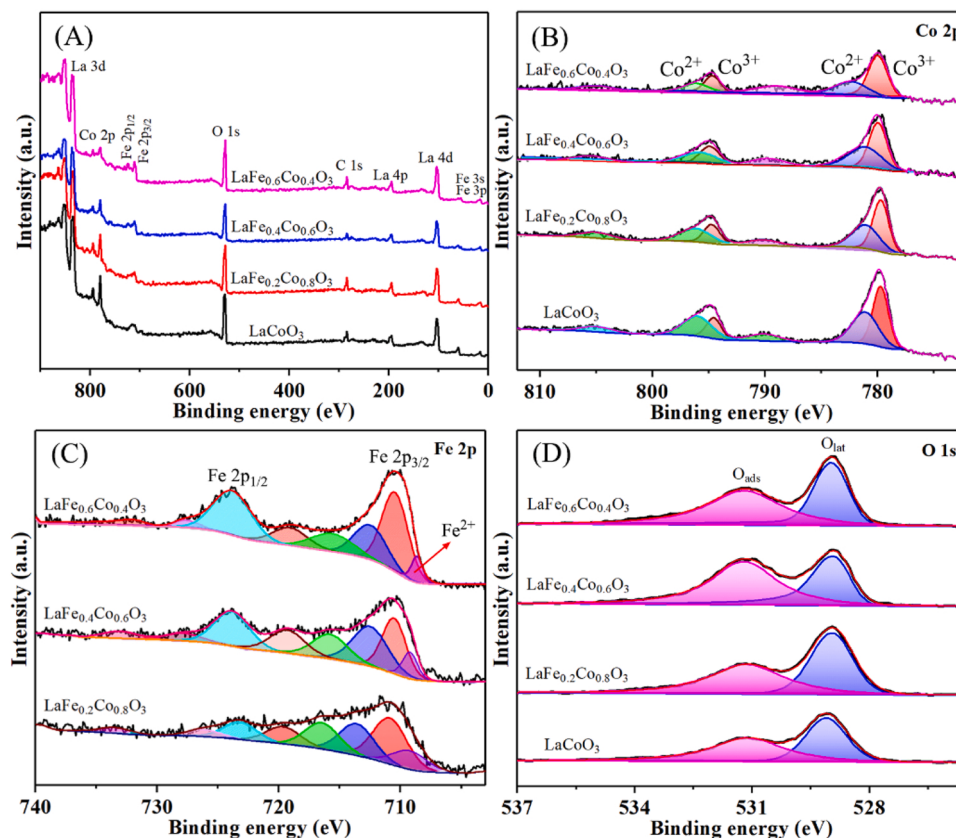
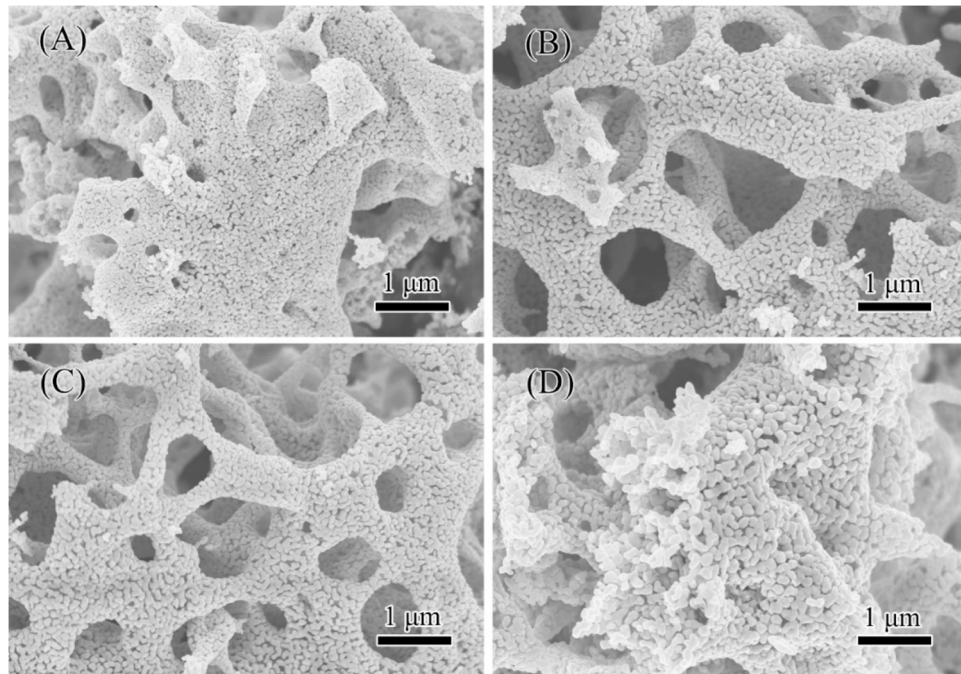
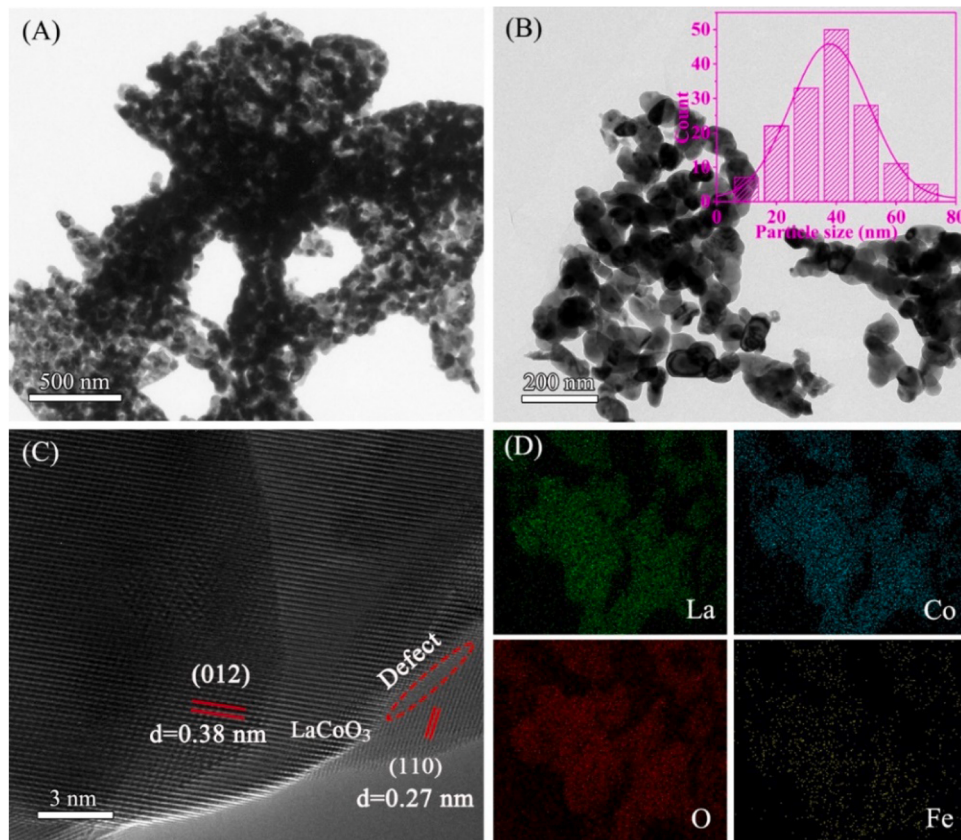


Fig. 2. (A) Survey scans, (B) Co 2p, (C) Fe 2p, and (D) O 1 s XPS spectra of LaFe<sub>x</sub>Co<sub>1-x</sub>O<sub>3</sub> catalysts.



**Fig. 3.** SEM images of  $\text{LaFe}_x\text{Co}_{1-x}\text{O}_3$  catalysts: (A)  $\text{LaCoO}_3$ , (B)  $\text{LaFe}_{0.2}\text{Co}_{0.8}\text{O}_3$ , (C)  $\text{LaFe}_{0.4}\text{Co}_{0.6}\text{O}_3$  and (D)  $\text{LaFe}_{0.6}\text{Co}_{0.4}\text{O}_3$ . (The acceleration voltage, current and magnification value of SEM images are 5 kV, 7  $\mu\text{A}$  and 20000X, respectively).



**Fig. 4.** (A, B) TEM images, (C) HRTEM image and (D) EDX maps (La, Co, O and Fe) of  $\text{LaFe}_{0.4}\text{Co}_{0.6}\text{O}_3$  catalyst.

results indicates that the actual mole content of metal elements is close to the theoretical addition amount.

### 3.2. Catalytic performance

The catalytic activities in the  $\text{H}_2\text{S}$  oxidation over perovskites were evaluated as a function of temperature under a WHSV of

9000 mL·g<sup>-1</sup>·h<sup>-1</sup>. As illustrated in Fig. 5A, the LaCoO<sub>3</sub> catalyst shows 81% H<sub>2</sub>S conversion at 220 °C. After depositing iron on LaCoO<sub>3</sub>, the catalytic activities of the catalysts are significantly improved. Among all the as-prepared catalysts, the LaFe<sub>0.4</sub>Co<sub>0.6</sub>O<sub>3</sub> catalyst achieves the complete H<sub>2</sub>S conversion at 190 °C. Meanwhile, the LaFe<sub>0.4</sub>Co<sub>0.6</sub>O<sub>3</sub> catalyst presents nearly 100% S selectivity in the whole reaction temperature ranges (Fig. 5B). The S selectivity of LaCoO<sub>3</sub>, LaFe<sub>0.2</sub>Co<sub>0.8</sub>O<sub>3</sub> and LaFe<sub>0.6</sub>Co<sub>0.4</sub>O<sub>3</sub> decreases from 100% to 85%, 91% and 95% at 220 °C, which results from the side reactions (S + O<sub>2</sub> → SO<sub>2</sub> and 2H<sub>2</sub>S + 3O<sub>2</sub> → 2H<sub>2</sub>O + 2SO<sub>2</sub>) [35]. Fig. 5C depicts the S yield of the as-obtained perovskite catalysts. With the increase of temperature, the S yield of LaFe<sub>0.4</sub>Co<sub>0.6</sub>O<sub>3</sub> raises and reaches 100% at 190 °C. LaCoO<sub>3</sub>, LaFe<sub>0.2</sub>Co<sub>0.8</sub>O<sub>3</sub> and LaFe<sub>0.6</sub>Co<sub>0.4</sub>O<sub>3</sub> show 69%, 91% and 95% S yield at 220 °C, respectively. The formation of product sulfur is confirmed by the yellow solid obtained from the effluent (Fig. S5). The above results demonstrate that the Fe modification improves the catalytic performance of perovskite in H<sub>2</sub>S selective oxidation.

The H<sub>2</sub>S conversions ( $X_{H_2S} < 20\%$ ) of LaFe<sub>x</sub>Co<sub>1-x</sub>O<sub>3</sub> perovskites for the evaluation of apparent activation energy ( $E_a$ ) and reaction rate are presented in Table S2, and the corresponding Arrhenius plots are displayed in Fig. 5D. Based on the slope of the Arrhenius plot, the apparent activation energy value of the catalysts increases in the order of LaFe<sub>0.4</sub>Co<sub>0.6</sub>O<sub>3</sub> (26.8 kJ/mol) < LaFe<sub>0.6</sub>Co<sub>0.4</sub>O<sub>3</sub> (33.5 kJ/mol) < LaFe<sub>0.2</sub>Co<sub>0.8</sub>O<sub>3</sub> (42.3 kJ/mol) < LaCoO<sub>3</sub> (56.3 kJ/mol), in consistent with their catalytic activity. Additionally, the reaction rates of catalysts were also calculated, which follows the order of LaFe<sub>0.4</sub>Co<sub>0.6</sub>O<sub>3</sub> ( $4.37 \times 10^{-3}$  mol·g<sup>-1</sup>·s<sup>-1</sup>) > LaFe<sub>0.6</sub>Co<sub>0.4</sub>O<sub>3</sub> ( $3.92 \times 10^{-3}$  mol·g<sup>-1</sup>·s<sup>-1</sup>) > LaFe<sub>0.2</sub>Co<sub>0.8</sub>O<sub>3</sub> ( $3.61 \times 10^{-3}$  mol·g<sup>-1</sup>·s<sup>-1</sup>) > LaCoO<sub>3</sub> ( $3.03 \times 10^{-3}$

mol·g<sup>-1</sup>·s<sup>-1</sup>). Being the lowest in  $E_a$  value and the largest in reaction rate, LaFe<sub>0.4</sub>Co<sub>0.6</sub>O<sub>3</sub> is the most active catalyst among the LaFe<sub>x</sub>Co<sub>1-x</sub>O<sub>3</sub> perovskites. These results highlight the impact of Fe modification of LaFe<sub>x</sub>Co<sub>1-x</sub>O<sub>3</sub> perovskites for H<sub>2</sub>S selective oxidation.

The LaFe<sub>0.4</sub>Co<sub>0.6</sub>O<sub>3</sub> catalyst was selected to study the effect of H<sub>2</sub>S/O<sub>2</sub> molar ratio, WHSV, water vapor and SO<sub>2</sub> on catalytic activity. The effect of H<sub>2</sub>S/O<sub>2</sub> molar ratio is illustrated in Fig. 6A. With the decrease of H<sub>2</sub>S/O<sub>2</sub> molar ratio from 3:1 to 1:2, the H<sub>2</sub>S conversion of LaFe<sub>0.4</sub>Co<sub>0.6</sub>O<sub>3</sub> increases from 89% to nearly 100% and then keeps stable, whereas the sulfur selectivity decreases from 100% to 88%. These results demonstrate that insufficient oxygen supply leads to low H<sub>2</sub>S conversion, while excess O<sub>2</sub> causes the decrease of S selectivity since it favors the deep oxidation of H<sub>2</sub>S [36]. Namely, a stoichiometric proportion (H<sub>2</sub>S/O<sub>2</sub> molar ratio is 2:1) facilitates the H<sub>2</sub>S selective oxidation over the LaFe<sub>x</sub>Co<sub>1-x</sub>O<sub>3</sub> perovskites. As shown in Fig. 6B, the S selectivity of LaFe<sub>0.4</sub>Co<sub>0.6</sub>O<sub>3</sub> keeps constant at 100% at WHSV below 10, 500 mL·g<sup>-1</sup>·h<sup>-1</sup>, and then decreases to 91% at 13,500 mL·g<sup>-1</sup>·h<sup>-1</sup>. Nearly a unity conversion H<sub>2</sub>S efficiency of about 100% is achieved at WHSV = 9000 mL·g<sup>-1</sup>·h<sup>-1</sup>, and it gradually decreases with the rise of WHSV. The results indicate that WHSV largely influence the catalytic performance in H<sub>2</sub>S selective oxidation.

Industrial H<sub>2</sub>S-containing exhaust usually contains H<sub>2</sub>O and SO<sub>2</sub>, which leads to the deactivation of catalysts [37]. Therefore, the effect of H<sub>2</sub>O and SO<sub>2</sub> on the catalytic performance over LaFe<sub>0.4</sub>Co<sub>0.6</sub>O<sub>3</sub> and LaCoO<sub>3</sub> was investigated at 220 °C (Fig. 6C). After the introduction of 10 vol% H<sub>2</sub>O, the H<sub>2</sub>S conversion of LaFe<sub>0.4</sub>Co<sub>0.6</sub>O<sub>3</sub> and LaCoO<sub>3</sub> gradually decrease ( $\Delta X_{H_2S} = 8.9\%$  and 14.7%). Then H<sub>2</sub>O was shut down and SO<sub>2</sub> (500 ppm) was introduced to the reactor. The H<sub>2</sub>S conversion of

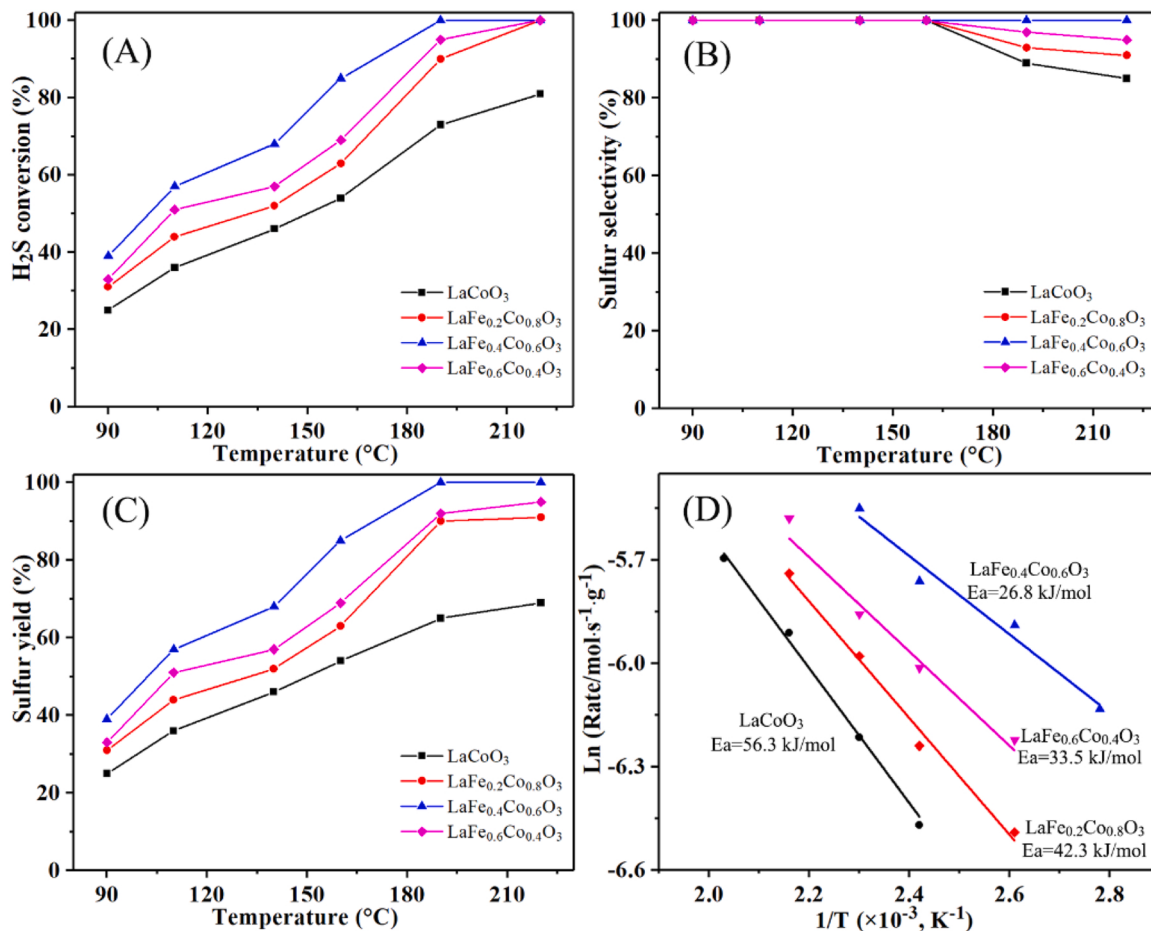


**Fig. 5.** (A) H<sub>2</sub>S conversion, (B) sulfur selectivity, (C) sulfur yield, and (D) Arrhenius plots for H<sub>2</sub>S oxidation of LaFe<sub>x</sub>Co<sub>1-x</sub>O<sub>3</sub> perovskites. Test conditions: H<sub>2</sub>S/O<sub>2</sub>/N<sub>2</sub> = 0.5/0.25/99.25 wt%, m = 0.2 g, WHSV = 9000 mL·g<sup>-1</sup>·h<sup>-1</sup>, v = 30 mL·min<sup>-1</sup>.

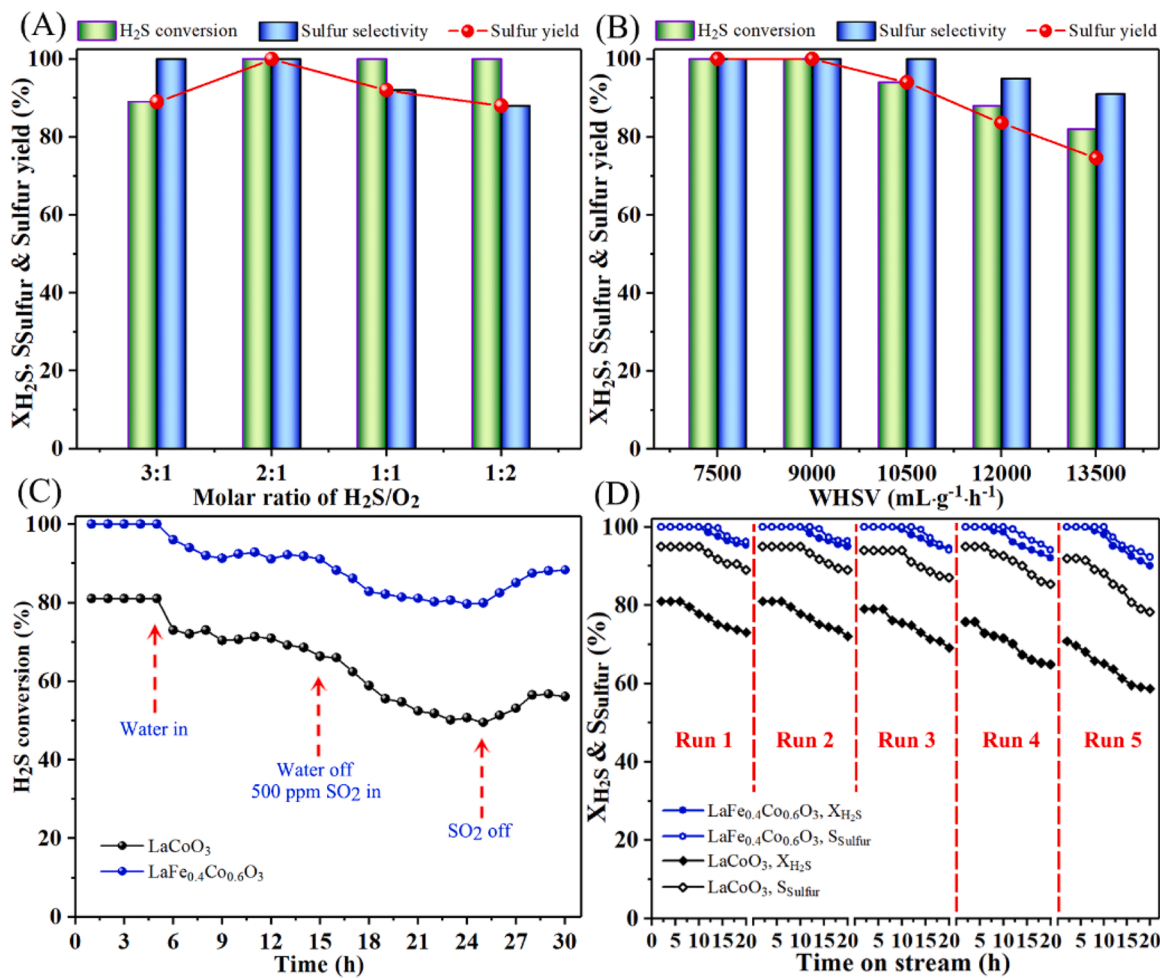


**Fig. 6.** Effect of (A) H<sub>2</sub>S/O<sub>2</sub> molar ratio and (B) WHSV on the catalytic activities of LaFe<sub>0.4</sub>Co<sub>0.6</sub>O<sub>3</sub>; (C) 10 vol% H<sub>2</sub>O and 500 ppm SO<sub>2</sub> tolerance tests and (D) cyclic stability of LaFe<sub>0.4</sub>Co<sub>0.6</sub>O<sub>3</sub> (S<sub>Sulfur</sub> and X<sub>H2S</sub> are the S selectivity and H<sub>2</sub>S conversion).

LaFe<sub>0.4</sub>Co<sub>0.6</sub>O<sub>3</sub> and LaCoO<sub>3</sub> continue to decrease ( $\Delta X_{H2S} = 11.4\%$  vs 16.8%) and recovers to 88.3% and 56.1% after the removal of SO<sub>2</sub>, respectively. The partial deactivation of the catalyst is caused by the competition between H<sub>2</sub>O/SO<sub>2</sub> and H<sub>2</sub>S at the active sites [38]. The result implies that LaFe<sub>0.4</sub>Co<sub>0.6</sub>O<sub>3</sub> exhibits better SO<sub>2</sub> and H<sub>2</sub>O resistance than LaCoO<sub>3</sub>. Fig. 6D depicts the catalytic stability of LaFe<sub>0.4</sub>Co<sub>0.6</sub>O<sub>3</sub> and LaCoO<sub>3</sub> at 220 °C. The H<sub>2</sub>S conversion of LaFe<sub>0.4</sub>Co<sub>0.6</sub>O<sub>3</sub> was kept at 100% for 10 h and then decreased gradually to 95.1%, while that of LaCoO<sub>3</sub> decreased from 81% to 72.1% during the 20 h reaction.

To investigate the cyclic stability of LaFe<sub>0.4</sub>Co<sub>0.6</sub>O<sub>3</sub>, the used sample was regenerated by calcined at 350 °C under N<sub>2</sub> (30 mL·min<sup>-1</sup>) for 90 min to remove elemental sulfur and then calcined at 600 °C under 30 mL·min<sup>-1</sup> airflow (21% O<sub>2</sub> and 79% N<sub>2</sub>) for 90 min to decompose ferric sulfate [39]. As shown in Fig. 6D, the H<sub>2</sub>S conversion of LaFe<sub>0.4</sub>Co<sub>0.6</sub>O<sub>3</sub> and LaCoO<sub>3</sub> keeps stable at 100% and 81.2% for 10 h and 6 h in the first run, respectively. During the first two regenerations, the stability of LaCoO<sub>3</sub> and LaFe<sub>0.4</sub>Co<sub>0.6</sub>O<sub>3</sub> remain unchanged, while there is only a slight decline of H<sub>2</sub>S conversion and S selectivity over these two catalysts after the third run. This result indicates that the deposited sulfur and sulfate could be effectively removed through the initial staged regeneration process. After fifth run, the LaFe<sub>0.4</sub>Co<sub>0.6</sub>O<sub>3</sub> exhibits 90.1% H<sub>2</sub>S conversion and 92.3% S selectivity, whereas those of LaCoO<sub>3</sub> are 56.1% and 78.3%. This phenomenon may be due to the accumulation of sulfate in the pores caused by the long-time reaction, which is difficult to remove completely by regeneration, and thus leads to the decrease in the number of active sites and the decline of catalytic activities. The data also suggest that Fe-doping promotes the recycled catalytic activity for

the H<sub>2</sub>S selective oxidation.

Note that the catalytic activities for H<sub>2</sub>S selective oxidation over LaFe<sub>0.4</sub>Co<sub>0.6</sub>O<sub>3</sub> are better than that of many reported materials in the literature. As for H<sub>2</sub>S conversion, the LaFe<sub>0.4</sub>Co<sub>0.6</sub>O<sub>3</sub> in our work displayed 100% H<sub>2</sub>S conversion at 190 °C. However, many reported works cannot achieve 100% H<sub>2</sub>S conversion. For instance, FeO<sub>x</sub>/GFC synthesized by Mikinen et al. displayed 95% H<sub>2</sub>S conversion at 250 °C [S1], and Fe/Al<sub>2</sub>O<sub>3</sub> prepared by Nguyen et al. exhibited 97.7% H<sub>2</sub>S conversion at 250 °C [S2]. On the other hand, the LaFe<sub>0.4</sub>Co<sub>0.6</sub>O<sub>3</sub> showed 100% S selectivity and yield under the feed gas of H<sub>2</sub>S/O<sub>2</sub>/N<sub>2</sub> = 0.5/0.25/99.25. However, under the same reaction gas condition, many works got poor results. For example, Zheng et al. reported the synthesis of MIL-53 (Fe), which displayed 92% S selectivity and yield at 180 °C [S3]. 5% V<sub>2</sub>O<sub>5</sub>/Ce-Lap catalyst synthesized by Zhang et al. displayed 88% S yield at 220 °C [S4]. For catalytic stability of H<sub>2</sub>S oxidation, the synthesized LaFe<sub>0.4</sub>Co<sub>0.6</sub>O<sub>3</sub> maintained 100% H<sub>2</sub>S conversion for 10 h and then decreased gradually to 95.1% after reaction for 20 h under H<sub>2</sub>S/O<sub>2</sub>/N<sub>2</sub> = 0.5/0.25/99.25. Ghasemy et al. reported the synthesis of Mo15/N-CNT nanocatalyst, which displayed 92% H<sub>2</sub>S conversion and S selectivity after reaction for 10 h under the feed gas of H<sub>2</sub>S/O<sub>2</sub>/N<sub>2</sub> = 0.3/0.15/99.55 [S5]. The 8%Fe/Zr-Lap catalyst prepared by Zhang et al. exhibited 98.5% H<sub>2</sub>S conversion for 10 h at 180 °C under H<sub>2</sub>S/O<sub>2</sub>/N<sub>2</sub> = 0.5/0.25/99.25 [S6]. The regeneration property of catalysts is also an important aspect of catalytic performance. In the present work, the LaFe<sub>0.4</sub>Co<sub>0.6</sub>O<sub>3</sub> still exhibited 90.1% H<sub>2</sub>S conversion and 92.3% S selectivity after five rounds of regeneration-testing under WHSV = 9000 mL·g<sup>-1</sup>·h<sup>-1</sup>. Lei et al. studied the catalytic performance of

graphitic carbon nitride for  $\text{H}_2\text{S}$  oxidation, which only showed 80% S yield after five regenerations under  $\text{WHSV} = 3000 \text{ mL}\cdot\text{g}^{-1}\cdot\text{h}^{-1}$  [S7]. Overall, the as-synthesized  $\text{LaFe}_{0.4}\text{Co}_{0.6}\text{O}_3$  exhibits excellent performance for  $\text{H}_2\text{S}$  selective oxidation.

### 3.3. Catalytic mechanisms

#### 3.3.1. Oxidation-reduction properties and *in-situ* characterizations

It is accepted that the reducibility and active oxygen species of perovskites are crucial for their catalytic reactivity. Therefore, we applied  $\text{H}_2\text{-TPR}$  and  $\text{O}_2\text{-TPD}$  measurements to assess these properties of the  $\text{LaFe}_x\text{Co}_{1-x}\text{O}_3$  perovskites. The  $\text{H}_2\text{-TPR}$  profiles were illustrated in Fig. 7A. For  $\text{LaCoO}_3$ , a weak peak below 300 °C is ascribed to the reduction of adsorbed oxygen species. Two peaks located at 366 and 620 °C could be assigned to the reduction of  $\text{Co}^{3+} \rightarrow \text{Co}^{2+}$  and  $\text{Co}^{2+} \rightarrow \text{Co}^0$ , respectively [40]. As for  $\text{LaFe}_x\text{Co}_{1-x}\text{O}_3$  perovskites, new peaks appear at around 400 and 680 °C, which are related to the stepwise reduction of  $\text{Fe}^{3+} \rightarrow \text{Fe}^{2+}$  and  $\text{Fe}^{2+} \rightarrow \text{Fe}^0$ , respectively [41]. Compared with  $\text{LaCoO}_3$ , the peaks ascribed to the reduction of Co ions over  $\text{LaFe}_x\text{Co}_{1-x}\text{O}_3$  perovskites shift to lower temperatures. This implies that Fe-doping improves the mobility of oxygen species and the reduction of cobalt species, finally promoting the redox property of  $\text{LaFe}_x\text{Co}_{1-x}\text{O}_3$  perovskites [42]. According to the location of the reduction temperatures, the  $\text{LaFe}_{0.4}\text{Co}_{0.6}\text{O}_3$  catalyst exhibits the highest reducibility.

To determine the oxygen species in the  $\text{LaFe}_x\text{Co}_{1-x}\text{O}_3$  perovskites, the  $\text{O}_2\text{-TPD}$  measurements were performed and the results are presented in Fig. 7B. The  $\text{O}_2\text{-TPD}$  profiles are divided into three types of peaks at 50–300, 300–600 and 600–900 °C, which are ascribed to the physisorbed oxygen on the surface, the chemisorbed oxygen on the oxygen vacancies, and the lattice oxygen [43]. As for the  $\text{LaFe}_{0.4}\text{Co}_{0.6}\text{O}_3$  catalyst, the desorption peak assigned to the surface lattice oxygen appears at 710 °C, which is lower than that of  $\text{LaCoO}_3$ . This result indicates that

Fe-doping would improve the mobility of surface lattice oxygen. Thereafter, active lattice oxygen is easy to react with  $\text{H}_2\text{S}$ , oxidizing it into sulfur at reaction temperature. Among the  $\text{LaFe}_x\text{Co}_{1-x}\text{O}_3$  perovskites,  $\text{LaFe}_{0.4}\text{Co}_{0.6}\text{O}_3$  exhibits the largest desorption peak area of chemisorbed oxygen. In general, oxygen vacancies are the reactive sites to adsorb, activate, and migrate the oxygen species [44,52]. That is,  $\text{LaFe}_{0.4}\text{Co}_{0.6}\text{O}_3$  exhibits the largest concentration of oxygen vacancies, which is consistent with the XPS results. During the reaction of  $\text{H}_2\text{S}$  oxidation, gaseous  $\text{O}_2$  could be dissociated and transferred into active lattice oxygen at oxygen vacancies, which enhances the oxygen mobility to effectively oxidize  $\text{H}_2\text{S}$  [45]. The metal-oxygen binding energy and oxygen mobility would be affected by the difference of electronegativity between metal and oxygen. The electronegativity of Fe, Co and O are 1.83, 1.88 and 3.44, respectively. The larger electronegativity difference of Fe and O causes the Co 3d energy band to be closer to the O 2p orbital, which increases the covalent component and promotes oxygen mobility.

To study the reaction pathway of  $\text{H}_2\text{S}$  oxidation, we conducted an *in-situ* FT-IR analysis of  $\text{H}_2\text{S}/\text{O}_2$  co-adsorption on  $\text{LaFe}_{0.4}\text{Co}_{0.6}\text{O}_3$  (Fig. 7C). After adsorption at 100 °C, new adsorption peaks corresponding to the adsorbed  $\text{H}_2\text{S}$  ( $\delta_{\text{HSH}}$ ) are detected at 1208 and 1407  $\text{cm}^{-1}$ . As for the reaction at 150 °C, a new peak assigned to the water ( $\delta_{\text{HOH}}$ ) appears at 1638  $\text{cm}^{-1}$ , which correlates to the reaction between  $\text{H}_2\text{S}$  and  $\text{O}_2$  ( $\text{H}_2\text{S} + 1/2 \text{O}_2 \rightarrow \text{S} + \text{H}_2\text{O}$ ). With the increase of reaction temperature (180 °C), the peak intensity of  $\text{H}_2\text{O}$  decreases due to the desorption of  $\text{H}_2\text{O}$  at high temperatures. After the reaction at 220 °C, several new peaks located at 800–1050  $\text{cm}^{-1}$  could be related to the sulfate species [46]. The result demonstrates that the high temperature causes the formation of sulfates resulting from the decrease of sulfur selectivity.

*In-situ* Raman spectra of  $\text{H}_2\text{S}/\text{O}_2$  adsorption were performed further to disclose the reaction process of  $\text{H}_2\text{S}$  oxidation. As illustrated in Fig. 7D, the Raman spectrum at 150 °C presents two weak bands ascribed to the elemental S at 216 ( $\nu_2$ ) and 468  $\text{cm}^{-1}$  ( $\nu_1$ ), which could

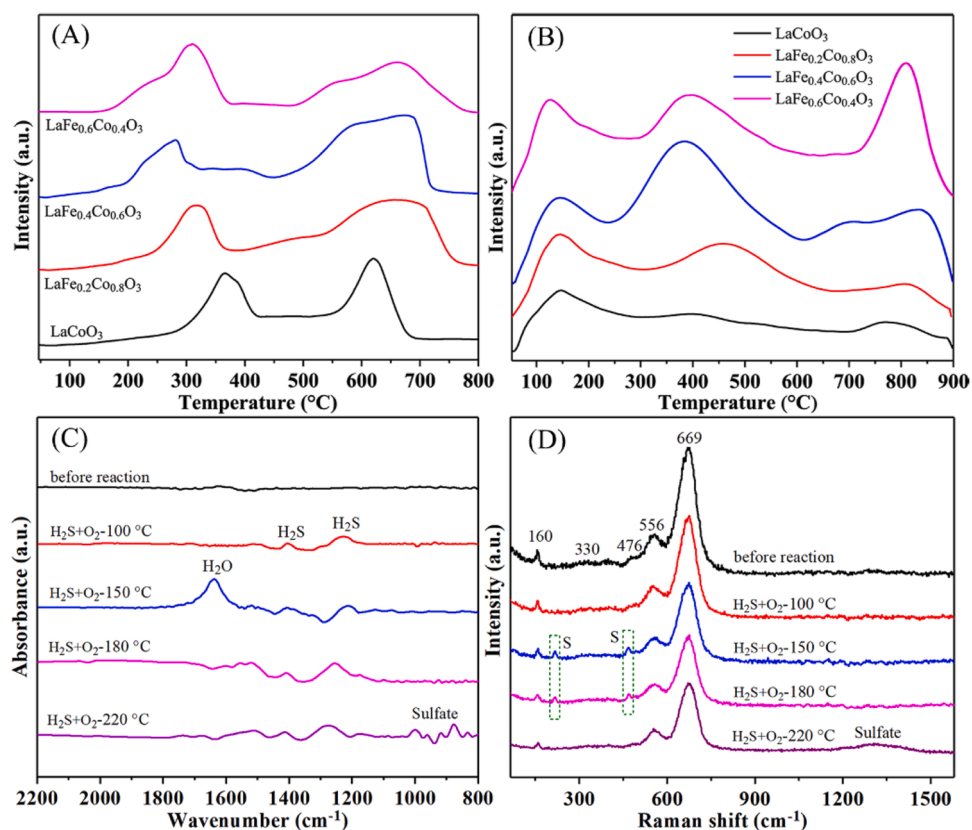


Fig. 7. (A)  $\text{H}_2\text{-TPR}$  profiles and (B)  $\text{O}_2\text{-TPD-MS}$  profiles of  $\text{LaFe}_x\text{Co}_{1-x}\text{O}_3$  perovskites; (C) *in-situ* FT-IR and (D) *in-situ* Raman spectra of  $\text{H}_2\text{S}/\text{O}_2$  adsorption over  $\text{LaFe}_{0.4}\text{Co}_{0.6}\text{O}_3$  performed at different temperatures.

be formed by the reaction of  $\text{H}_2\text{S} + 1/2 \text{O}_2 \rightarrow \text{S} + \text{H}_2\text{O}$  [47]. The Raman band of sulfur is still maintained after the reaction at 180 °C, implying the further reaction of  $\text{H}_2\text{S}$  selective oxidation. Further increase of reaction temperature (220 °C) causes the formation of sulfates ( $1390 \text{ cm}^{-1}$ ), which agrees well with the result of *in-situ* FT-IR experiment. Additionally, the deposition of sulfur and  $\text{H}_2\text{O}$  on the window of *in situ* pool also verifies the selective oxidation of  $\text{H}_2\text{S}$  on the  $\text{LaFe}_{0.4}\text{Co}_{0.6}\text{O}_3$  perovskite (Fig. S6).

### 3.3.2. DFT calculations and reaction mechanism

As shown in Fig. 8A and B, a  $(2 \times 2 \times 2)$  supercell was used to simulate the  $\text{LaCoO}_3$ , where the Co atoms are six-fold coordinated. The average Co-O bond length is 1.91 Å in the optimized structure. The formation energy of oxygen vacancy ( $E_{\text{vac}}$ ) for  $\text{LaCoO}_3$  was calculated by the formula:  $E_{\text{vac}} = E_{\text{LaCoO}_3-x} - E_{\text{LaCoO}_3} + 0.5E_{\text{O}_2}$ , where  $E_{\text{O}_2}$  means the energy of  $\text{O}_2$  molecule,  $E_{\text{LaCoO}_3-x}$  and  $E_{\text{LaCoO}_3}$  represent the total energy of  $\text{LaCoO}_3$  with and without an  $\text{O}_v$ . The calculated  $E_{\text{vac}}$  value of pure  $\text{LaCoO}_3$  is 2.72 eV. After the introduction of an iron atom into the structure (Fig. 8C), the six Fe-O bonds possess an average bond length of 1.92 Å. After optimization calculation, the most stable Fe-doped  $\text{LaCoO}_{3-x}$  with an  $\text{O}_v$  is presented in Fig. 8D, and the calculated  $E_{\text{vac}}$  value is 1.82 eV. The decrease of  $E_{\text{vac}}$  value indicates that the Fe doping facilitates the formation of oxygen defects over  $\text{LaCoO}_3$  [48].

DFT calculations were conducted to study the adsorption behaviors of  $\text{H}_2\text{S}$  on the defective Fe-doped  $\text{LaCoO}_3$  surface. Fig. S7 depicts four models for  $\text{H}_2\text{S}$  adsorption at Fe, Co,  $\text{O}_v$  and O sites of the Fe-doped  $\text{LaCoO}_3$  surface. The calculated data show that V- $\text{H}_2\text{S}(\text{O}_v)$  is the most energetically stable configuration. In this structure,  $\text{H}_2\text{S}$  is atop an  $\text{O}_v$  site with a  $\text{H}_2\text{S}$  adsorption energy of  $-0.63$  eV. This result indicates that  $\text{H}_2\text{S}$  prefers to be adsorbed to the  $\text{O}_v$  site [49]. The dissociation process of  $\text{H}_2\text{S}$  on the defective Fe-doped  $\text{LaCoO}_3$  surface was also investigated. As displayed in Fig. 8E,  $\text{H}_2\text{S}$  adsorption on the  $\text{O}_v$  site is chosen as the initial state. The S-H bond lengths of adsorbed  $\text{H}_2\text{S}$  are 1.352 Å and 1.356 Å, larger than that of a free  $\text{H}_2\text{S}$  (1.328 Å), indicating the breakage of S-H bond. After the fracture of S-H bond in absorbed  $\text{H}_2\text{S}$ , the first dissociation procedure ( $\text{H}_2\text{S} \rightarrow \text{H} + \text{SH}$ ) occurs with a dissociation energy of  $-0.98$  eV. Subsequently, the second dissociation process ( $\text{SH} \rightarrow \text{H} + \text{S}$ ) proceeds with a dissociation energy of  $-0.51$  eV. The negative values suggest that the  $\text{H}_2\text{S}$  dissociation on the defective Fe-doped  $\text{LaCoO}_3$  surface process is favorable.

As above discussed, we proposed a possible reaction pathway (Mars-van Krevelen mechanism) for the  $\text{H}_2\text{S}$  selective oxidation on the  $\text{LaFe}_x\text{Co}_{1-x}\text{O}_3$  perovskites. As presented in Fig. 9,  $\text{H}_2\text{S}$  molecule diffuses into the pores and adsorbs on the surface oxygen vacancy. The adsorbed  $\text{H}_2\text{S}$  is oxidized to S by the surface lattice oxygen near the  $\text{O}_v$  site with the formation of a synergistic oxygen vacancy. Then the synergistic oxygen vacancy is replenished by feed  $\text{O}_2$ , leaving an oxygen adatom ( $\text{O}_{\text{ads}}$ ) outside the synergistic oxygen vacancy [50]. Finally, the adsorbed  $\text{O}_{\text{ads}}$  could be abstracted by  $\text{H}_2\text{S}$  to form the second sulfur.

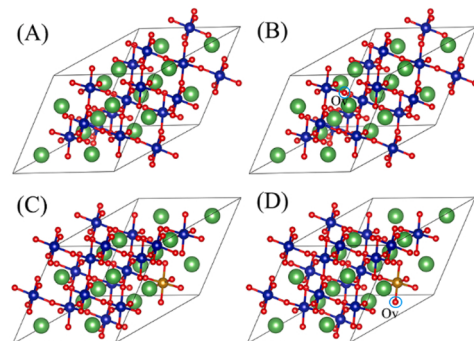


**Fig. 8.** The optimized structures of (A) pure  $\text{LaCoO}_3$  and (B) the most stable structure for pure  $\text{LaCoO}_3$  with an  $\text{O}_v$ ; (C) Fe-doped  $\text{LaCoO}_3$ , (D) the most stable structure for Fe-doped  $\text{LaCoO}_3$  with an  $\text{O}_v$ ; (E) Schematic of energy profile of  $\text{H}_2\text{S}$  dissociation on defective Fe-doped  $\text{LaCoO}_3$  surface. (Red, blue, green and yellow spheres represent O, Co, La and Fe atoms, respectively. The blue circle represents the  $\text{O}_v$  site.).

### 3.4. Catalyst stability

To elucidate the reason that is responsible for catalyst deactivation, the used  $\text{LaFe}_{0.4}\text{Co}_{0.6}\text{O}_3$  catalyst was characterized by XRD, XPS and SEM. As depicted in Fig. 10A, the XRD pattern of the used  $\text{LaFe}_{0.4}\text{Co}_{0.6}\text{O}_3$  catalyst is similar to that of the fresh sample, indicating the phase structure was maintained well during the reaction. The SEM image of the used catalyst shown in Fig. 10B further certifies the structural stability of  $\text{LaFe}_{0.4}\text{Co}_{0.6}\text{O}_3$ . It is obvious that the  $\text{O}_{\text{ads}}/\text{O}_{\text{total}}$  ratio of the used catalyst increased from 0.64 to 0.88 after the stability test (Fig. 10C), implying that  $\text{O}_{\text{lat}}$  species were involved in the reaction. The  $\text{S} 2p$  XPS spectra illustrated in Fig. 10D indicate that there are two discernible sulfur components on the used catalyst, the peaks at 163.4 and 168.9 eV are related to the elemental S and sulfate, respectively [51]. The result demonstrates that the deposition of sulfate and sulfur results in the decrease of  $\text{H}_2\text{S}$  oxidation activity.

## 4. Conclusions

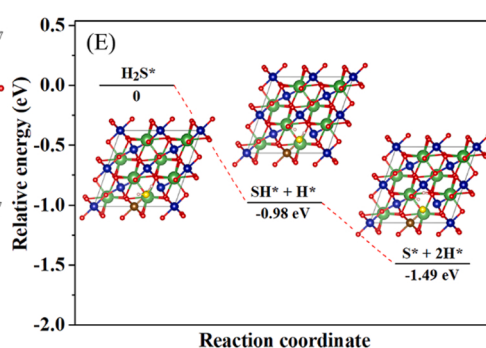
In summary, a series of  $\text{LaFe}_x\text{Co}_{1-x}\text{O}_3$  perovskites were synthesized via a citric acid assisted sol-gel method. The substitution of Co by Fe at the B sites reduces the formation energy of oxygen vacancy and increases the  $\text{O}_v$  concentration, which facilitates the  $\text{H}_2\text{S}$  adsorption and promotes oxygen mobility that benefits the  $\text{H}_2\text{S}$  selective oxidation. Among the  $\text{LaFe}_x\text{Co}_{1-x}\text{O}_3$  perovskite catalysts,  $\text{LaFe}_{0.4}\text{Co}_{0.6}\text{O}_3$  perovskite exhibited an optimized  $\text{H}_2\text{S}$  conversion and S selectivity of 100% at 190 °C. The results of DFT calculations also demonstrate that Fe-doping enhances the formation of  $\text{O}_v$  and the adsorption of  $\text{H}_2\text{S}$ . The findings provide deep insights into designing high-performance perovskite catalysts for oxidative desulfurization.

## CRediT authorship contribution statement

**Xiaohai Zheng:** Conceptualization, Methodology, Funding acquisition, Investigation, Writing - original draft. **Bang Li :** Data curation. **Lijuan Shen :** Formal analysis. **Yanning Cao:** Supervision, Writing - review & editing. **Yingying Zhan:** Resources, Funding acquisition, Methodology. **Shoutian Zheng:** Resources, Formal analysis, Writing - review & editing. **Shiping Wang:** Data curation. **Lilong Jiang:** Supervision, Funding acquisition, Project administration, Resources.

## Declaration of Competing Interest

The authors declare that they have no known competing financial interests or personal relationships that could have appeared to influence the work reported in this paper.



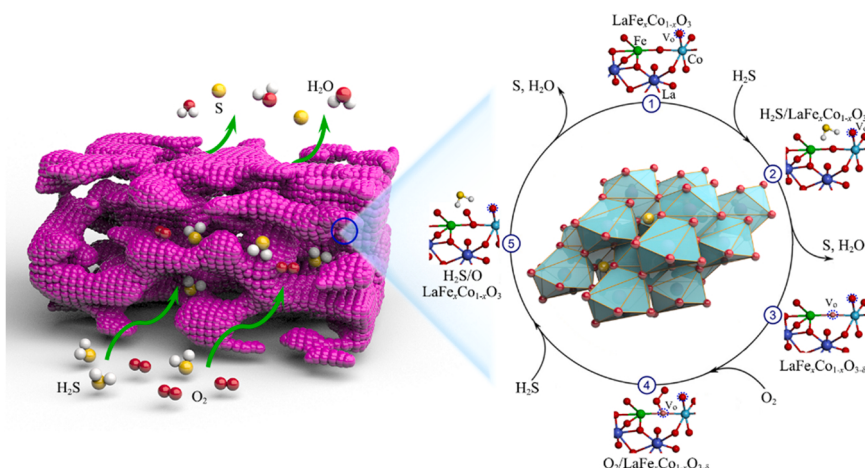


**Fig. 9.** Schematic of  $\text{H}_2\text{S}$  selective oxidation on the  $\text{LaFe}_{\text{x}}\text{Co}_{1-\text{x}}\text{O}_3$  perovskites.

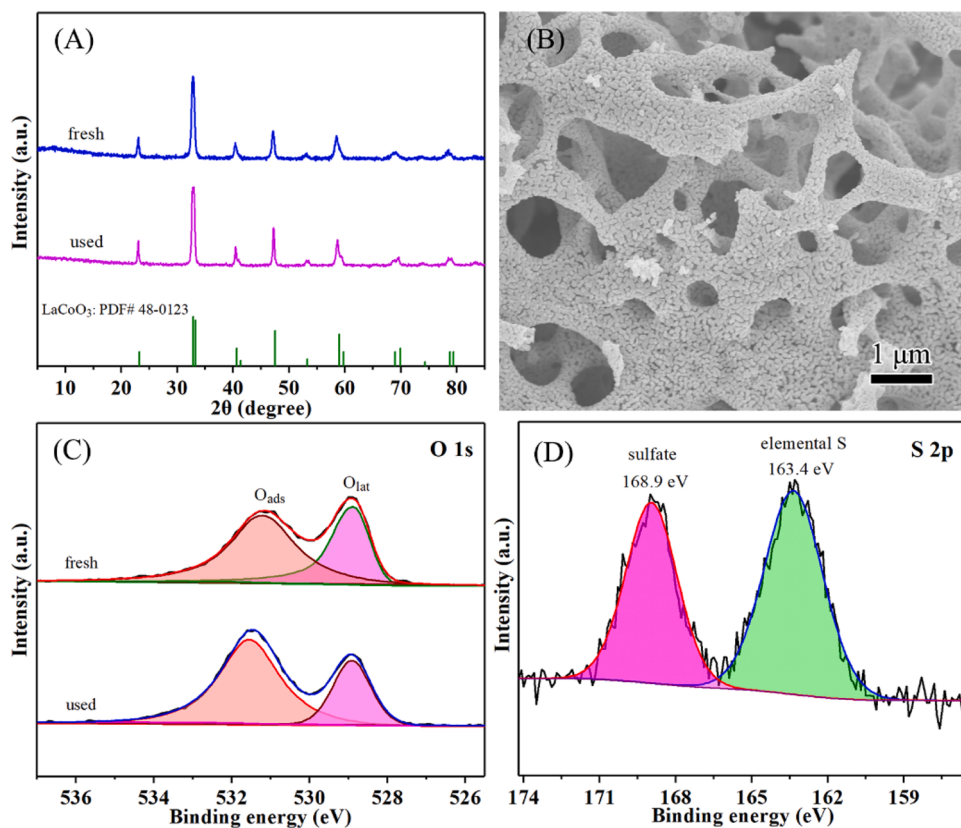


**Fig. 10.** (A) XRD patterns of as-prepared and used  $\text{LaFe}_{0.4}\text{Co}_{0.6}\text{O}_3$ ; (B) SEM image of used  $\text{LaFe}_{0.4}\text{Co}_{0.6}\text{O}_3$ ; (C) O 1s XPS spectra of as-prepared and used  $\text{LaFe}_{0.4}\text{Co}_{0.6}\text{O}_3$  and (D) S 2p XPS spectra of used  $\text{LaFe}_{0.4}\text{Co}_{0.6}\text{O}_3$  catalyst.

#### Data availability

The authors are unable or have chosen not to specify which data has been used.

#### Acknowledgements

The authors gratefully acknowledge the National Science Fund for Distinguished Young Scholars of China (21825801), National Natural Science Foundation of China (NSFC) (22178060, 22208060, 22278073 and 22208055), National Key Research and Development Program of China (2018YFA0209403), China Postdoctoral Science Foundation

(2022M720740), Qingyuan Innovation Laboratory Testing Fund of Precious Apparatus (QYT2023001) and Major Program of Qingyuan Innovation Laboratory (00121003).

#### Appendix A. Supporting information

Supplementary data associated with this article can be found in the online version at doi:10.1016/j.apcatb.2023.122526.

## References

- [1] Y. Pan, M. Chen, Z. Su, K. Wu, Y. Zhang, D. Long, Two-dimensional CaO/carbon heterostructures with unprecedented catalytic performance in room-temperature H<sub>2</sub>S oxidation, *Appl. Catal. B Environ.* 280 (2021), 119444.
- [2] S. Chen, Y. Guo, J. Zhang, Y. Guo, X. Liang, CuFe<sub>2</sub>O<sub>4</sub>/activated carbon adsorbents enhance H<sub>2</sub>S adsorption and catalytic oxidation from humidified air at room temperature, *Chem. Eng. J.* 431 (2022), 134097.
- [3] F. Zhang, Z. Wei, G. Jiang, G. Li, M. Zhao, Z. Zhang, J. Cheng, Z. Hao, Synergistic conversion of acid gases (H<sub>2</sub>S and CO<sub>2</sub>) to valuable chemicals: carbonyl sulfide synthesis over vacancy-defective CoMo sulfide catalysts, *Appl. Catal. B Environ.* 319 (2022), 121912.
- [4] S. Lyu, W. Wu, R. Xiong, C. Yang, B. Sa, J. Zhang, Y. Hou, X. Wang, Carbon-rich carbon nitride nanocatalysts for H<sub>2</sub>S selective oxidation, *J. Catal.* 413 (2022) 992–1004.
- [5] X. Zheng, J. Cai, Y. Cao, L. Shen, Y. Zheng, F. Liu, S. Liang, Y. Xiao, L. Jiang, Construction of cross-linked δ-MnO<sub>2</sub> with ultrathin structure for the oxidation of H<sub>2</sub>S: structure-activity relationship and kinetics study, *Appl. Catal. B Environ.* 297 (2021), 120402.
- [6] X. Zhang, Z. Wang, Y. Tang, N. Qiao, Y. Li, S. Qu, Z. Hao, Catalytic behaviors of combined oxides derived from Mg/Al<sub>x</sub>Fe<sub>1-x</sub>Cl layered double hydroxides for H<sub>2</sub>S selective oxidation, *Catal. Sci. Technol.* 5 (2015) 4991–4999.
- [7] X.Y. Zhang, L. Cui, D.H. An, J.P. Fu, J. Liu, Y. Dong, H<sub>2</sub>S-selective catalytic oxidation to sulfur over iron oxide sorbent supported on semi-Coke, *Energy Fuels* 34 (2020) 2315–2322.
- [8] X. Zheng, J. Cai, W. Zhao, S. Liang, Y. Zheng, Y. Cao, L. Shen, Y. Xiao, L. Jiang, Porous α-Fe<sub>2</sub>O<sub>3</sub>/SnO<sub>2</sub> nanoflower with enhanced sulfur selectivity and stability for H<sub>2</sub>S selective oxidation, *Chin. Chem. Lett.* 32 (2021) 2143–2150.
- [9] Y. Wang, H. Arandiyani, H.A. Tahini, J. Scott, X. Tan, H. Dai, J.D. Gale, A.L. Rohl, S. C. Smith, R. Amal, The controlled disassembly of mesostructured perovskites as an avenue to fabricating high performance nanohybrid catalysts, *Nat. Commun.* 8 (2017) 1–7.
- [10] Y. Xu, J. Dhainaut, J.-P. Dacquin, A.-S. Mamede, M. Marinova, J.-F. Lamoulier, H. Vezin, H. Zhang, S. Royer, La<sub>1-x</sub>(Sr, Na, K)<sub>x</sub>MnO<sub>3</sub> perovskites for HCHO oxidation: the role of oxygen species on the catalytic mechanism, *Appl. Catal. B Environ.* 287 (2021), 119955.
- [11] X. Zheng, Y. Li, S. Liang, Z. Yao, Y. Zheng, L. Shen, Y. Xiao, Y. Zhang, C. Au, L. Jiang, Promoting effect of Cu-doping on catalytic activity and SO<sub>2</sub> resistance of porous CeO<sub>2</sub> nanorods for H<sub>2</sub>S selective oxidation, *J. Catal.* 389 (2020) 382–399.
- [12] H. Wang, X. Dong, T. Zhao, H. Yu, M. Li, Dry reforming of methane over bimetallic Ni-Co catalyst prepared from La(Co<sub>x</sub>Ni<sub>1-x</sub>)<sub>0.5</sub>Fe<sub>0.5</sub>O<sub>3</sub> perovskite precursor: catalytic activity and coking resistance, *Appl. Catal. B Environ.* 245 (2019) 302–313.
- [13] Y. Zheng, Y. Chen, E. Wu, X. Liu, B. Huang, H. Xue, C. Cao, Y. Luo, Q. Qian, Q. Chen, Amorphous boron dispersed in LaCoO<sub>3</sub> with large oxygen vacancies for efficient catalytic propane oxidation, *Chem. Eur. J.* 27 (2021) 4738–4745.
- [14] Y. Li, C. Yang, H. Fan, Y. Wang, M. Duan, Y. Feng, J. Lin, Enhanced sulfur selectivity for H<sub>2</sub>S catalytic oxidation over Fe<sub>2</sub>O<sub>3</sub>/UiO-66 catalyst, *Sep. Purif. Technol.* 289 (2022), 120791.
- [15] M. Sun, X. Wang, Y. Li, Z. Zhao, J. Qiu, Selective catalytic oxidation of pollutant H<sub>2</sub>S over Co-decorated hollow N-doped carbon nanofibers for high-performance Li-S batteries, *Appl. Catal. B Environ.* 317 (2022), 121763.
- [16] G. Kresse, J. Hafner, Ab initio molecular-dynamics simulation of the liquid-metal-amorphous-semiconductor transition in germanium, *Phys. Rev. B* 49 (1994) 14251.
- [17] G. Kresse, J. Furthmüller, Efficiency of ab-initio total energy calculations for metals and semiconductors using a plane-wave basis set, *Comp. Mater. Sci.* 6 (1996) 15–50.
- [18] T. Wang, C. Zhang, J. Wang, H. Li, Y. Duan, Z. Liu, J.Y. Lee, X. Hu, S. Xi, Y. Du, The interplay between the suprafacial and intrafacial mechanisms for complete methane oxidation on substituted LaCoO<sub>3</sub> perovskite oxides, *J. Catal.* 390 (2020) 1–11.
- [19] P. Ciambelli, S. Cimino, S. De Rossi, L. Lisi, G. Minelli, P. Porta, G. Russo, AFeO<sub>3</sub> (A=La, Nd, Sm) and LaFe<sub>1-x</sub>Mg<sub>x</sub>O<sub>3</sub> perovskites as methane combustion and CO oxidation catalysts: structural, redox and catalytic properties, *Appl. Catal. B Environ.* 29 (2001) 239–250.
- [20] P. Ciambelli, S. Cimino, L. Lisi, M. Faticanti, G. Minelli, I. Pettiti, P. Porta, La, Ca and Fe oxide perovskites: preparation, characterization and catalytic properties for methane combustion, *Appl. Catal. B Environ.* 33 (2001) 193–203.
- [21] A. Bhalla, R. Guo, R. Roy, The perovskite structure-a review of its role in ceramic science and technology, *Mater. Res. Innov.* 4 (2000) 3–26.
- [22] H. Liu, B. Guo, K. Zheng, R. Xie, X. Zhang, X. Wu, Y. Zhang, C. Li, Novel visible-light-driven photoconductive properties of LaCoO<sub>3</sub> epitaxial nano-thin films, *Mater. Lett.* 209 (2017) 446–449.
- [23] S. Ajmal, I. Bibi, F. Majid, S. Ata, K. Kamran, K. Jilani, S. Nouren, S. Kamal, A. Ali, M. Iqbal, Effect of Fe and Bi doping on LaCoO<sub>3</sub> structural, magnetic, electric and catalytic properties, *J. Mater. Res. Technol.* 8 (2019) 4831–4842.
- [24] H. Liu, W. Jia, X. Yu, X. Tang, X. Zeng, Y. Sun, T. Lei, H. Fang, T. Li, L. Lin, Vitamin C-assisted synthesized Mn-Co oxides with improved oxygen vacancy concentration: boosting lattice oxygen activity for the air-oxidation of 5-(hydroxymethyl)furfural, *ACS Catal.* 11 (2021) 7828–7844.
- [25] L. Kang, B. Wang, Q. Bing, M. Zalibera, R. Büchel, R. Xu, Q. Wang, Y. Liu, D. Gianolio, C.C. Tang, Adsorption and activation of molecular oxygen over atomic copper (I/II) site on ceria, *Nat. Commun.* 11 (2020) 1–11.
- [26] J.-C. Ding, H.-Y. Li, Z.-X. Cai, X.-D. Zhang, X. Guo, LaCoO<sub>3</sub>-based sensors with high sensitivity to carbon monoxide, *RSC Adv.* 5 (2015) 65668–65673.
- [27] Y. Zhang, H. Liu, H. Hu, R. Xie, G. Ma, J. Huo, H. Wang, Orientation-dependent structural and photocatalytic properties of LaCoO<sub>3</sub> epitaxial nano-thin films, *Roy. Soc. Open Sci.* 5 (2018), 171376.
- [28] J.G. Kim, Y. Kim, Y. Noh, S. Lee, Y. Kim, W.B. Kim, Bifunctional hybrid catalysts with perovskite LaCo<sub>0.8</sub>Fe<sub>0.2</sub>O<sub>3</sub> nanowires and reduced graphene oxide sheets for an efficient Li-O<sub>2</sub> battery cathode, *ACS Appl. Mater. Interfaces* 10 (2018) 5429–5439.
- [29] H. Chang, E. Bjørgum, O. Mihai, J. Yang, H.L. Lein, T. Grande, S. Raaen, Y.-A. Zhu, A. Holmen, D. Chen, Effects of oxygen mobility in La-Fe-based perovskites on the catalytic activity and selectivity of methane oxidation, *ACS Catal.* 10 (2020) 3707–3719.
- [30] M. Sathiya, G. Rousse, K. Ramesha, C.P. Laisa, H. Vezin, M.T. Sougrati, M. L. Doublet, D. Foix, D. Gonbeau, W. Walker, A.S. Prakash, M. Ben Hassine, L. Dupont, J.M. Tarascon, Reversible anionic redox chemistry in high-capacity layered-oxide electrodes, *Nat. Mater.* 12 (2013) 827–835.
- [31] H. Wang, Z. Qu, H. Xie, N. Maeda, L. Miao, Z. Wang, Insight into the mesoporous Fe<sub>x</sub>Ce<sub>1-x</sub>O<sub>2-δ</sub> catalysts for selective catalytic reduction of NO with NH<sub>3</sub>: regulable structure and activity, *J. Catal.* 338 (2016) 56–67.
- [32] P. García-Muñoz, C. Lefevre, D. Robert, N. Keller, Ti-substituted LaFeO<sub>3</sub> perovskite as photoassisted CWPO catalyst for water treatment, *Appl. Catal. B Environ.* 248 (2019) 120–128.
- [33] W. Li, Y. Hu, H. Jiang, N. Jiang, W. Bi, C. Li, Litchi-peel-like hierarchical hollow copper-ceria microspheres: aerosol-assisted synthesis and high activity and stability for catalytic CO oxidation, *Nanoscale* 10 (2018) 22775–22786.
- [34] Y. Shen, M.J.M. de Vidales, G. Gorni, M.J. Rivero, I. Ortiz, A.J. Dos santos-García, Enhanced peroxyxonosulfate activation in the morphotropic phase boundary of molybdenum doped LaCoO<sub>3-δ</sub> perovskite, *Chem. Eng. J.* (2022), 137352.
- [35] S. Li, Y. Liu, H. Gong, K.-H. Wu, H. Ba, C. Duong-Viet, C. Jiang, C. Pham-Huu, D. Su, N-doped 3D mesoporous carbon/carbon nanotubes monolithic catalyst for H<sub>2</sub>S selective oxidation, *ACS Appl. Nano Mater.* 2 (2019) 3780–3792.
- [36] F. Zhang, X. Zhang, Z. Hao, G. Jiang, H. Yang, S. Qu, Insight into the H<sub>2</sub>S selective catalytic oxidation performance on well-mixed Ce-containing rare earth catalysts derived from MgAlCe layered double hydroxides, *J. Hazard. Mater.* 342 (2018) 749–757.
- [37] K.V. Bineesh, D.-K. Kim, M.-I. Kim, M. Selvaraj, D.-W. Park, Design, synthesis and characterization of vanadia-doped iron-oxide pillared montmorillonite clay for the selective catalytic oxidation of H<sub>2</sub>S, *Dalton Trans.* 40 (2011) 3938–3945.
- [38] X. Zheng, G. Zhang, Z. Yao, Y. Zheng, L. Shen, F. Liu, Y. Cao, S. Liang, Y. Xiao, L. Jiang, Engineering of crystal phase over porous MnO<sub>2</sub> with 3D morphology for highly efficient elimination of H<sub>2</sub>S, *J. Hazard. Mater.* 411 (2021), 125180.
- [39] M. Wu, T. Li, H. Li, H. Fan, J. Mi, Desulfurization of hot coal gas over regenerable low-cost Fe<sub>2</sub>O<sub>3</sub>/mesoporous Al<sub>2</sub>O<sub>3</sub> prepared by the sol-gel method, *Energy Fuels* 31 (2017) 13921–13932.
- [40] Y. Luo, Y. Zheng, X. Feng, D. Lin, Q. Qian, X. Wang, Y. Zhang, Q. Chen, X. Zhang, Controllable P doping of the LaCoO<sub>3</sub> catalyst for efficient propane oxidation: optimized surface Co distribution and enhanced oxygen vacancies, *ACS Appl. Mater. Interfaces* 12 (2020) 23789–23799.
- [41] X. Zheng, Y. Li, Y. Zheng, L. Shen, Y. Xiao, Y. Cao, Y. Zhang, C.-T. Au, L. Jiang, Highly efficient porous Fe<sub>x</sub>Ce<sub>1-x</sub>O<sub>2-δ</sub> with three-dimensional hierarchical nanoflower morphology for H<sub>2</sub>S-selective oxidation, *ACS Catal.* 10 (2020) 3968–3983.
- [42] J.A. Onrubia-Calvo, B. Pereda-Ayo, I. Cabrejas, U. De-La-Torre, J.R. González-Velasco, Ba-doped vs. Sr-doped LaCoO<sub>3</sub> perovskites as base catalyst in diesel exhaust purification, *Mol. Catal.* 488 (2020), 110913.
- [43] S. Wang, X. Xu, J. Zhu, D. Tang, Z. Zhao, Effect of preparation method on physicochemical properties and catalytic performances of LaCoO<sub>3</sub> perovskite for CO oxidation, *J. Rare Earth.* 37 (2019) 970–977.
- [44] J. Yang, S. Hu, L. Shi, S. Hoang, W. Yang, Y. Fang, Z. Liang, C. Pan, Y. Zhu, L. Li, Oxygen vacancies and lewis acid sites synergistically promoted catalytic methane combustion over perovskite oxides, *Environ. Sci. Technol.* 55 (2021) 9243–9254.
- [45] T. Gao, J. Chen, W. Fang, Q. Cao, W. Su, F. Dumégnil, Ru/Mn<sub>x</sub>Ce<sub>1-x</sub>O<sub>y</sub> catalysts with enhanced oxygen mobility and strong metal-support interaction: exceptional performances in 5-hydroxymethylfurfural base-free aerobic oxidation, *J. Catal.* 368 (2018) 53–68.
- [46] S. Kataoka, E. Lee, M.I. Tejedor-Tejedor, M.A. Anderson, Photocatalytic degradation of hydrogen sulfide and in situ FT-IR analysis of reaction products on surface of TiO<sub>2</sub>, *Appl. Catal. B Environ.* 61 (2005) 159–163.
- [47] T. Raabe, H. Rasser, S. Nottebaum, A. Groß, H. Krause, S. Kureti, Mechanistic study on H<sub>2</sub>S and subsequent O<sub>2</sub> adsorption on iron oxides and hydroxides, *Appl. Surf. Sci.* 565 (2021), 150504.
- [48] X. Zheng, Y. Li, L. Zhang, L. Shen, Y. Xiao, Y. Zhang, C. Au, L. Jiang, Insight into the effect of morphology on catalytic performance of porous CeO<sub>2</sub> nanocrystals for H<sub>2</sub>S selective oxidation, *Appl. Catal. B Environ.* 252 (2019) 98–110.
- [49] S. Zhao, L. Ling, B. Wang, R. Zhang, D. Li, Q. Wang, J. Wang, Theoretic insight into the desulfurization mechanism: removal of H<sub>2</sub>S by ceria (110), *J. Phys. Chem. C* 119 (2015) 7678–7688.
- [50] X. Zheng, Y. Li, W. You, G. Lei, Y. Cao, Y. Zhang, L. Jiang, Construction of Fe-doped TiO<sub>2-x</sub> ultrathin nanosheets with rich oxygen vacancies for highly efficient oxidation of H<sub>2</sub>S, *Chem. Eng. J.* 430 (2021), 132917.
- [51] C. Yang, H. Ye, J. Byun, Y. Hou, X. Wang, N-rich carbon catalysts with economic feasibility for the selective oxidation of hydrogen sulfide to sulfur, *Environ. Sci. Technol.* 54 (2020) 12621–12630.
- [52] X. Zheng, P. Yu, Y. Liu, Y. Ma, Y. Cao, Z. Cai, L. Zhou, K. Huang, S. Zheng, L. Jiang, Efficient Hydrogenation of Methyl Palmitate to Hexadecanol over Cu/m-ZrO<sub>2</sub> Catalysts: Synergistic Effect of Cu Species and Oxygen Vacancies, *ACS Catal.* 13 (2023) 2047–2060.